THE JOURNAL OF
PHYSICAL CHEMISTRY C

pubs.acs.org/JPCC Article

# Unraveling the $Eu^{2+} \rightarrow Mn^{2+}$ Energy Transfer Mechanism in w-LED Phosphors

Atul D. Sontakke,* Arnoldus J. van Bunningen, Freddy T. Rabouw, Sam Meijers, and Andries Meijerink*

**Cite This:** *J. Phys. Chem. C* 2020, 124, 13902−13911 Read Online

ACCESS | Metrics & More | Article Recommendations | Supporting Information

**ABSTRACT:** Recent research on white light LED (w-LED) phosphors has focused on narrow-band green and red luminescent materials to improve the efficacy of w-LEDs and to widen the color gamut of w-LED-based displays. $Mn^{2+}$ is a promising emitter capable of narrow-band emission, either green or red, depending on the local coordination. However, the extremely low absorption coefficients for the spin- and parity-forbidden d−d transitions in $Mn^{2+}$ form a serious drawback and require addition of a sensitizer ion such as $Ce^{3+}$ or $Eu^{2+}$, with strong absorption in the blue. The performance of the codoped phosphor then critically depends on efficient energy transfer. Despite extensive research, a clear understanding of the $Eu^{2+} \rightarrow Mn^{2+}$ and $Ce^{3+} \rightarrow Mn^{2+}$ transfer mechanism is lacking. Typically, Dexter exchange interaction or electric dipole−quadrupole coupling are considered. Here we investigate $Eu^{2+} \rightarrow Mn^{2+}$ energy transfer in $Ba_2MgSi_2O_7$ and show that the most probable mechanism is exchange interaction with fast (nanoseconds) energy transfer from $Eu^{2+}$ to nearest-neighbor $Mn^{2+}$ and much slower (>100 ns) transfer to next-nearest neighbors, as expected for exchange interaction. We critically evaluate previous studies where the assignment of dipole−quadrupole interaction was erroneously based on $C_{Mn}^{8/3}$ concentration dependence of energy transfer efficiencies. Preferential $Eu^{2+}$−$Mn^{2+}$ pair formation is suggested as a mechanism that enhances energy transfer efficiencies.

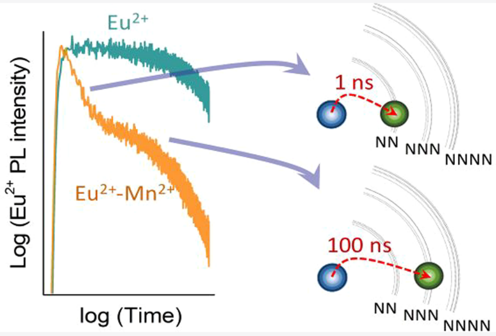

## ■ INTRODUCTION

Narrow-band emitting phosphors are of great current interest.[1] Narrow-band red emission around 610−630 nm enables higher efficacy (improved lumen/watt output) of warm w-LEDs in comparison to w-LEDs with broad-band red phosphors.[2,3] These broad-band red emitters suffer from efficacy losses as a significant part of the emission is in the spectral range beyond 630 nm, where the eye sensitivity significantly drops. In displays with w-LED backlights, narrow-band red (NBR) and narrow-band green (NBG) emission widens the color gamut and allows for a higher brightness by using narrow-band emission that matches the displays' color filter transmission. A promising candidate for narrow-band red or green emission is $Mn^{2+}$ ($3d^5$), and this ion therefore gained huge interest as an activator ion.[4,5] The d−d intraconfigurational $^4T_1$−$^6A_1$ emission of $Mn^{2+}$ is typically in the green/orange spectral region for $Mn^{2+}$ in tetrahedral coordination and in the orange/red spectral region in octahedral coordination (higher crystal field strength). Unfortunately, the d−d absorption strength in the blue is extremely low, making singly doped $Mn^{2+}$ phosphors unsuitable for (In,Ga)N-based LED excitation. Absorption transitions from the $^6A_1$ ground state to the $^4T_1$ and $^4T_2$ excited states of $Mn^{2+}$ are spin- and parity-forbidden. To tackle the weak d−d absorption, codoping with sensitizers having allowed transitions (f−d in $Eu^{2+}$, $Ce^{3+}$; s−p in $Sn^{2+}$, $Sb^{3+}$, $Pb^{2+}$, $Bi^{3+}$) with effective absorption of blue excitation light can be the solution if efficient nonradiative energy transfer to $Mn^{2+}$ ions can be realized.[6−12]

Sensitized $Mn^{2+}$ emission has widely been investigated in many host matrices.[6−35] The mechanism for $Ce^{3+}$−$Mn^{2+}$ and $Eu^{2+}$−$Mn^{2+}$ energy transfer is not clear: both electric dipole−quadrupole and Dexter exchange interaction have been proposed.[13] As electric dipole transitions are strongly forbidden in $Mn^{2+}$, dipole−dipole interaction is considered as inefficient. Dipole−quadrupole interaction can be efficient at short interaction ranges and has a $r^{-8}$ distance dependence. Unlike Coulombic multipole interactions, a direct calculation of exchange transfer rates is difficult.[13] However, its distance dependence significantly differs from that of Coulomb interactions. The transfer rate depends on wave function overlap and follows an exponential distance dependence. It is typically only efficient at short distances, below 5 Å. In early work by Soules et al.[10] on $Sb^{3+}$−$Mn^{2+}$ transfer in halophosphate and by Stevels et al.[13] on $Eu^{2+}$−$Mn^{2+}$ transfer in $\beta$-alumina, it was demonstrated that exchange interaction is

**Received:** April 17, 2020
**Revised:** June 2, 2020
**Published:** June 3, 2020

the most likely mechanism, but dipole−quadrupole interaction could not be excluded. The high efficiency of energy transfer in NaCl codoped with $Eu^{2+}$ and $Mn^{2+}$ was attributed to the preferential formation of sensitizer−$Mn^{2+}$ pairs by Rubio et al. as effective energy transfer occurred even at ppm doping levels in NaCl.[14−16]

In recent work, dipole−quadrupole interaction has consistently been favored as energy transfer mechanism.[32−54] The $r^{-8}$ distance dependence of this interaction was used as evidence. With reference to a pioneering paper on concentration quenching in inorganic solids by Dexter and Schulman,[55] a $C_{Mn}{}^{8/3}$ dependence of the ratio $I_{S0}/I_S$ was taken as evidence for dipole−quadrupole interaction, where $I_{S0}$ is the $Eu^{2+}$ emission intensity in singly $Eu^{2+}$ doped materials and $I_S$ is the intensity in $Eu^{2+}$−$Mn^{2+}$ codoped materials. Plots of $I_{S0}/I_S$ (or alternatively the ratio of Eu emission lifetimes $\tau_{S0}/\tau_S$) vs $C_{Mn}{}^{8/3}$ gave better linear fits than plots vs $C_{Mn}{}^{6/3}$ (dipole−dipole) or $C_{Mn}{}^{10/3}$ (quadrupole−quadrupole). Accordingly, the dipole−quadrupole type interaction was proposed in a wide variety of $Eu^{2+}$−$Mn^{2+}$ codoped compounds. Similar conclusions were made for $Ce^{3+}$−$Mn^{2+}$ energy transfer. Still, a few reports proposed electron exchange interactions responsible for sensitized $Mn^{2+}$ emission.[27−31]

Dexter predicted exchange transfer rate to be high, about $10^{10}$−$10^{11}$ $s^{-1}$ for donor−acceptor separations of 4 Å.[56] This high probability and the close proximity of $Eu^{2+}$ ions to nearest $Mn^{2+}$ neighbors (4−5 Å) in many of the codoped hosts make it somewhat surprising that exchange interaction as sensitization mechanism is not commonly found in recent reports. As the sensitized $Mn^{2+}$ emission possesses high potential in achieving narrow-band LED phosphors, it is vital to resolve the sensitization mechanism.

Here we present a detailed analysis of $Eu^{2+}$−$Mn^{2+}$ energy transfer in $Ba_2MgSi_2O_7$ at cryogenic (4.2 K) and ambient (300 K) temperature. Steady-state photoluminescence (PL) and time-resolved PL decay kinetics provide complementary information about the energy transfer efficiency and mechanism. Analysis of the $Eu^{2+}$ emission decay kinetics using subnanosecond time resolution provides evidence for an ultrafast decay component that is easily overlooked in typical lifetime measurements. The fast decay component is assigned to ∼1 ns energy transfer to nearest $Mn^{2+}$ neighbors. The much slower transfer observed for transfer to next-nearest neighbors shows that efficient $Eu^{2+}$−$Mn^{2+}$ energy transfer indeed occurs at short range with a dominant contribution from Dexter exchange interaction. Closer analysis of the Mn concentration dependence of the $I_{S0}/I_S$ ratio dependence reveals that for donor−acceptor transfer a linear dependence on the Mn concentration is expected, independent of the energy transfer mechanism. The concentration dependence for energy transfer efficiencies reported by Dexter and Schulman[55] was in fact not derived for donor−acceptor dipole−quadrupole transfer but as concentration dependence for "concentration quenching for activators having forbidden transitions". Concentration quenching of emission by donor−donor energy transfer (*not* donor−acceptor transfer) was shown to have a $C^{S/3}$ dependence with $S = 6$, 8, or 10 for dipole−dipole, dipole−quadrupole, and quadrupole−quadrupole interaction. This $C^{S/3}$ dependence has since then been used in many publications, especially in reports on $Eu^{2+} \rightarrow Mn^{2+}$ and $Ce^{3+} \rightarrow Mn^{2+}$ energy transfer, to determine the energy transfer mechanism for single-step donor−acceptor energy transfer, which is unfortunately incorrect. Both theory and experiment show that the donor−acceptor energy transfer rate scales linearly with the acceptor concentration.

## MATERIALS AND METHODS

**Synthesis.** $Ba_2MgSi_2O_7$ compounds were obtained by using the solid-state reaction method. Reagent grade precursor chemicals, $BaCO_3$, MgO, $SiO_2$, $Eu_2O_3$, and $MnCO_3$, were stoichiometrically weighed and mixed thoroughly by using an agate mortar and pestle. For doping, Ba ions were substituted for Eu and Mg ions for Mn as $Ba_{2(1-x)}Mg_{(1-y)}Si_2O_7$: $x$% Eu, $y$% Mn. The dopant concentrations were selected following the earlier reports on $Eu^{2+}$ and $Mn^{2+}$ singly doped $Ba_2MgSi_2O_7$ compounds, where the optimum luminescence intensity for individual ions was obtained for 3.5% $Eu^{2+}$ and 5% $Mn^{2+}$ dopant concentrations, respectively.[57−59] Accordingly, the $Eu^{2+}$ concentration was fixed at $x = 3.5\%$ and codoped with a series of $Mn^{2+}$ concentrations, $y = 0\%$, 1%, 3%, 5%, 7%, and 10%. The samples thus identified as 0% Mn, 1% Mn, 3% Mn, 5% Mn, 7% Mn, and 10% Mn based on Mn codoping percentages, unless stated otherwise. The well mixed chemical batches were pressed into pellets (13 mm diameter × 3 mm height) using 10 ton uniaxial pressure. The pellets were then introduced to resistive heating tube furnace in alumina boats, and a reducing atmosphere was applied. The heating was performed in two steps: At first, the temperature was increased to 800 °C at 5 °C/min ramp and then maintained at 800 °C for 1 h. Later, the temperature was raised to 1100 °C at 3 °C/min ramp rate and kept for 5 h. Finally, the temperature was decreased to 30 °C at 10 °C/min ramp rate. The pellets were crushed to fine powders.

**Experimental Methods.** The powders were examined by using powder X-ray diffraction for its phase purity. A Bruker D2 PHASER X-ray diffractometer with Co target ($\lambda_{K\alpha}$ = 1.78897 Å) was used at 30 kV operating voltage and 10 mA current. The step size resolution was 0.01° $2\theta$. The photoluminescence (PL) spectroscopy was performed by using an Edinburgh Instruments FLS-920 fluorescence spectrometer. The PL and PL excitation (PLE) measurements were recorded using a 450 W Xe lamp as excitation source and a Hamamatsu R928 photomultiplier tube (PMT) detector. The resolution was maintained at 0.5 nm for both PL and PLE measurements. For $Eu^{2+}$ PL decay measurement, a picosecond pulsed laser diode (Edinburgh Instruments EPL 375, peak wavelength: 376.5 nm; pulse width: 65 ps) was used as excitation source, and the signals were recorded by using a Hamamatsu H74220-60 fast response PMT. The decay curves were recorded by using the single-photon counting method with 4000 channels resolution. For a normal full range (10 μs) decay curve, each channel provides 2.4 ns resolution. For higher resolution (HR) decay measurements, the channel width was reduced to 0.048 ns. The $Eu^{2+}$ PL was monitored at 470 nm at 300 K and 500 nm at 4.2 K. $Mn^{2+}$ PL decay measurement was performed by using a tunable optical paramagnetic oscillator (OPO) Opotek Opolette HE 355II pulsed laser (pulse width: 10 ns; repetition rate: 10 Hz) as excitation source, and the emission was recorded by a Hamamatsu R928 PMT detector. For cryogenic (4.2 K) measurements, the samples were cooled by using an Oxford Instruments liquid He flow cryostat. For temperature dependence study, liquid He flow cryostat was employed in the 4.2−300 K temperature range, whereas a temperature-controlled stage from Linkam Scientific (THMS600) was used for the 300−700 K temperature range. For data analysis and plotting,

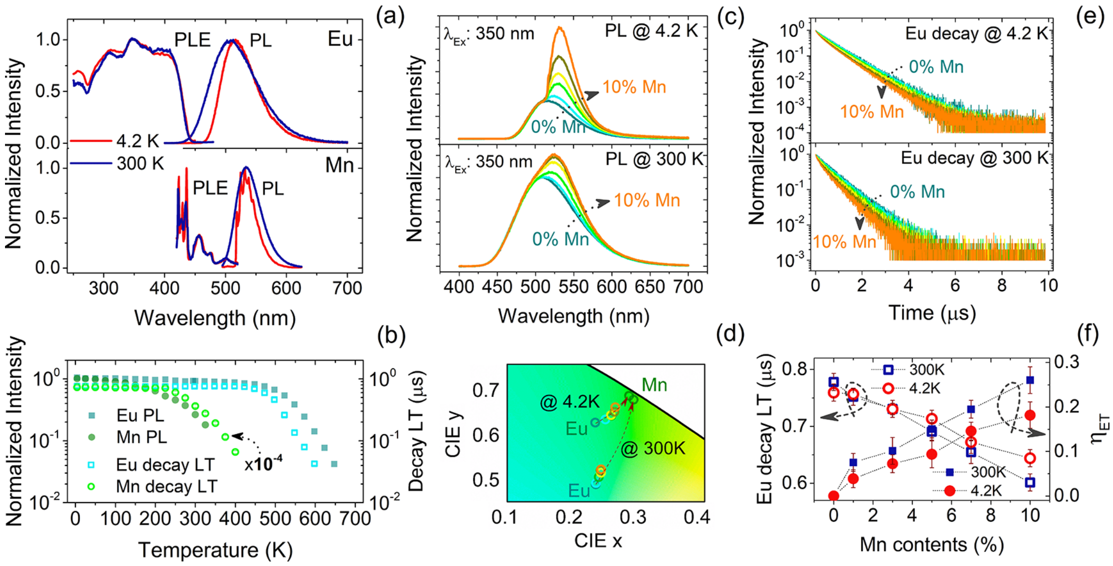

**Figure 1.** Emission and excitation spectra of $Eu^{2+}$ (3.5%) and $Mn^{2+}$ (7%) singly doped $Ba_2MgSi_2O_7$ (a). Temperature dependence of the $Eu^{2+}$ and $Mn^{2+}$ emission intensity and decay lifetime (LT) (b). Emission spectra of codoped $Ba_2MgSi_2O_7$:$Eu^{2+}$(3.5%),$Mn^{2+}$(0−10%) compounds at 4.2 and 300 K (c). Corresponding color evolution in CIE diagram for 0−10% Mn codoping (d). $Eu^{2+}$ luminescence decay curves for $Ba_2MgSi_2O_7$:$Eu^{2+}$(3.5%), $Mn^{2+}$(0−10%) ($\lambda_{em}$ = 470 nm at 300 K and 500 nm at 4.2 K, $\lambda_{exc}$ = 375 nm) (e). Average $Eu^{2+}$ emission decay lifetimes (LT) and energy transfer efficiencies ($\eta_{ET}$) (f) obtained at 4.2 and 300 K from the decay curves in (e).

Origin Lab (9.1 version) software was used. All curve fittings were performed by using orthogonal distance regression algorithms. The crystal structure and radial ionic distribution analysis was performed by using the VESTA (3.4.4 version) software.

## RESULTS AND DISCUSSION

In $Ba_2MgSi_2O_7$, $Eu^{2+}$ occupies $Ba^{2+}$ dodecahedral sites and $Mn^{2+}$ occupies $Mg^{2+}$ tetrahedral sites because of the charge and size similarity with the ions they substitute.[57−59] Figure 1a presents the PL and PL excitation (PLE) spectra of $Eu^{2+}$ and $Mn^{2+}$ singly doped $Ba_2MgSi_2O_7$ compounds recorded at 4.2 and 300 K. The $Eu^{2+}$ emission is in the cyan-green region (maximum around 515 nm at 4.2 K) and is assigned to the $4f^65d \rightarrow 4f^7$ transition. The corresponding excitation spectrum has an onset in the blue and covers the UV spectral region. The broad excitation band is the typical spectrum observed for $Eu^{2+}$ and corresponds to $4f^7 \rightarrow 4f^6(^7F_J)5d$ transitions. The $Mn^{2+}$ emission is a rather narrow band and situated in the green around 530 nm. At 4.2 K vibrational fine structure is observed which is characteristic for narrow-band emission with a small Stokes shift (small Huang−Rhys parameter $S$). Emission from both $Eu^{2+}$ and $Mn^{2+}$ shows thermal broadening. A blue-shift is also observed in $Eu^{2+}$ PL with increase in temperature, whereas the $Mn^{2+}$ PL exhibits a slight red-shift. The blue-shift of $Eu^{2+}$ emission with temperature was previously attributed to lattice expansion with increasing temperature.[58] Indeed, a larger distance between $Eu^{2+}$ and oxide ligands corresponds to a reduced crystal-field splitting of the $4f^65d^1$ excited state of $Eu^{2+}$. The emission from the lowest crystal-field component thus blue-shifts with increasing temperature. In addition, vibrational coupling increases with increasing temperature, thus broadening the emission profile. In contrast, for $Mn^{2+}$ a slight red-shift is observed with increasing temperature, which also agrees with earlier report.[59] The $Mn^{2+}$ d−d transitions are spin- and parity-forbidden. The spectrum is dominated by phonon sidebands, as Laporte's selection rules is relaxed for transitions between vibrational states (electron−phonon coupling).[60] The transition strengths of both Stokes and anti-Stokes sidebands increase with increasing temperature, depending on the phonon energies involved. The spectral shape thus changes in a nonstraightforward way. While at low temperatures individual vibronic lines are observed and determine the peak maximum, the vibronic lines broaden at elevated temperatures. It has been shown that this broadening of vibronic lines gives rise to a red-shift of the emission maximum[61] and can explain the observed slight red-shift in $Mn^{2+}$ PL in $Ba_2MgSi_2O_7$. The PLE profiles do not show significant changes with temperature.

The temperature dependence of integrated PL intensity and luminescence lifetime ($\tau$) for the $Eu^{2+}$ and $Mn^{2+}$ emission is presented in Figure 1b. The $Eu^{2+}$ PL is quite stable until 450 K, but the $Mn^{2+}$ PL starts to quench above 200 K. The thermal quenching has been attributed to the thermally induced ionization of excited state electrons in both cases.[58,59] The difference in temperature threshold is then due to the differences in energy separations between the excited state of the ions and the conduction band edge of the host. The decrease in PL intensity by thermal quenching coincides with a decrease in emission lifetime. For $Eu^{2+}$ the ~0.8 $\mu$s decay time starts to decrease rapidly above 450 K. For $Mn^{2+}$ a long 7.3 ms lifetime is observed at low temperatures. This is typical for the spin- and parity-forbidden $^4T_1$−$^6A_1$ emission of $Mn^{2+}$. When quenching sets in above 200 K, the additional nonradiative decay processes shorten the lifetime as expected. The luminescence quenching behavior of $Mn^{2+}$ is also reflected in the PL of $Eu^{2+}$−$Mn^{2+}$ codoped compounds (Figure 1c). Here, the 4.2 K spectra show a prominent contribution of sensitized $Mn^{2+}$ PL, but this becomes less significant at 300 K. Nevertheless, in both cases, the PL showed a steady rise of $Mn^{2+}$ component with increasing $Mn^{2+}$ concentration, which helps shift the color coordinates toward the green (Figure 1d). It is interesting to note that the 4.2 K vibronic fine structure observed in the $Mn^{2+}$ PL for the singly doped compound disappears in codoped compounds, which can be explained by an inhomogeneous broadening effect associated with $Eu^{2+}$−$Mn^{2+}$ pair formation.

The donor ($Eu^{2+}$) luminescence decay curves are presented in Figure 1e for different $Mn^{2+}$ codoping concentrations recorded at 4.2 and 300 K. After some initial faster decay, a single-exponential ∼0.8 $\mu$s decay is observed for singly $Eu^{2+}$ doped $Ba_2MgSi_2O_7$. The emission decay becomes faster and nonexponential upon codoping with $Mn^{2+}$. This is expected, as energy transfer to $Mn^{2+}$ becomes an alternative decay path for excited $Eu^{2+}$. Transfer rates vary and depend on the number of and distance to $Mn^{2+}$ neighbors for specific $Eu^{2+}$ ions, which explains the nonexponential character. The decrease in decay time is more pronounced at 300 K. This agrees well with the PL properties, which reveal increased spectral overlap of $Eu^{2+}$ emission with $Mn^{2+}$ absorption at 300 K, as the PL is more broadened and blue-shifted (Figure 1a). The average $Eu^{2+}$ emission decay times were obtained by multiexponential fitting of decay curves and are plotted in Figure 1f along with the related energy transfer efficiencies (see the Supporting Information, Figure S1 and Tables S1, S2). The energy transfer efficiency ($\eta_{ET}$) was calculated via the equation

$$\eta_{ET} = 1 - \frac{\tau_{DA}}{\tau_D} \qquad (1)$$

Here, $\tau_D$ and $\tau_{DA}$ represent the donor emission decay times in singly (D) and codoped (DA) compounds. The $\tau_D$ values of 0.79 $\mu$s at 4.2 K and 0.81 $\mu$s at 300 K were obtained from the exponential fit of emission decay in singly Eu doped compound at longer times (Table S1). Alternatively, the energy transfer efficiency can be derived from the integrated area under the decay curves in the codoped compounds in comparison to the exponential (radiative) decay. Both methods give similar values for the ET efficiency of about 18% at 4.2 K and 26% at 300 K for 10% $Mn^{2+}$ codoping (see Table S2).

It is interesting to note that the PL profiles of codoped compounds show significant contribution of sensitized $Mn^{2+}$ emission (Figure 1c). The relative intensity of the $Mn^{2+}$ emission is higher than expected for the transfer efficiency values determined from emission decay curves (Figure 1f), which appear to strongly underestimate the actual transfer efficiency. To quantify the difference, we determined the energy transfer efficiencies from the PL spectra. Figure 2a presents the deconvoluted steady-state PL photon flux spectra of codoped compounds. We used two different approaches to estimate the energy transfer efficiencies at 4.2 and 300 K using spectral data. At 4.2 K, the normalized photon fraction of $Eu^{2+}$ and $Mn^{2+}$ emission was used assuming that both $Eu^{2+}$ and $Mn^{2+}$ exhibit near-unity quantum efficiency. At 300 K, the $Mn^{2+}$ emission is partially quenched, and therefore the absolute photon counts of the $Eu^{2+}$ emission from PL relative intensities were determined as a function of $Mn^{2+}$ concentration (Figure 2b). The energy transfer efficiencies were obtained via the following expressions:

$$\eta_{ET@4.2K} = \frac{Mn^{2+}\ \text{photons}}{\text{total }(Eu^{2+} + Mn^{2+})\ \text{photons}} \qquad (2)$$

$$\eta_{ET@300K} = 1 - \frac{(Eu^{2+}\ \text{photons})_{DA}}{(Eu^{2+}\ \text{photons})_{D}} \qquad (3)$$

Here, the subscripts "D" and "DA" represent singly doped (donor only) and codoped (donor + acceptor) compounds, respectively. Figure 2c presents the transfer efficiencies at 4.2 and 300 K obtained by using spectral data, which shows about 53% at 4.2 K and 61% at 300 K for 10% $Mn^{2+}$ contents—far greater than those obtained from the analysis of luminescence decay curves.

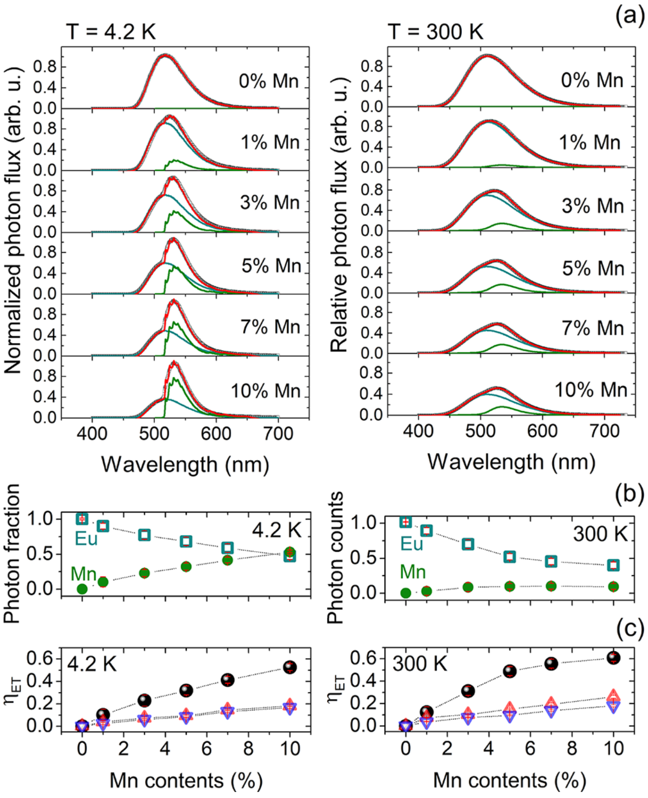

**Figure 2.** Deconvoluted PL photon flux spectra of $Eu^{2+}$ (3.5%) and $Mn^{2+}$ (0−10%) codoped $Ba_2MgSi_2O_7$ (a). Corresponding photon fractions and absolute photon counts for $Eu^{2+}$ and $Mn^{2+}$ emission as a function of $Mn^{2+}$ concentration (b) and the energy transfer efficiencies, $\eta_{ET}$ (c), obtained at 4.2 and 300 K. The deconvolution was performed by using $Eu^{2+}$ and $Mn^{2+}$ emission photon spectra in singly doped $Ba_2MgSi_2O_7$ at respective temperatures. In (c), the solid spheres represent $\eta_{ET}$ obtained by using spectral data. The $\eta_{ET}$ obtained from emission decay analysis is included based on multiexponential fits (△) and integration of luminescence decay curves (▽) (Table S2).

The results in Figure 1 and 2 reveal a clear inconsistency in energy transfer efficiency obtained by using luminescence decay measurements and spectral data with much higher transfer efficiencies derived from the spectral data (see Figure 2c). This is critical, as the former method is employed for energy transfer analysis in many previous reports.[26,44−54] To resolve the inconsistency, luminescence lifetime measurements were performed by using a much higher time resolution to resolve fast nearest-neighbor (NN) energy transfer in Eu−Mn pairs. Indications that fast NN transfer can go undetected for measurements relying on typical low time resolution measurements were given by Rubio et al., who reported that the $Eu^{2+}$ decay lifetimes in singly $Eu^{2+}$ doped and $Eu^{2+}$−$Mn^{2+}$ codoped NaCl compounds remain the same despite presence of intense sensitized $Mn^{2+}$ luminescence.[15] They argued that virtually all $Eu^{2+}$ ions transfer their energy to nearest-neighbor $Mn^{2+}$ ions, and this is too fast to be observed in the donor decay kinetics. Figure 3a presents the high-resolution (HR) PL decay curves (channel width 0.048 ns) of the $Eu^{2+}$ singly doped and $Eu^{2+}$−

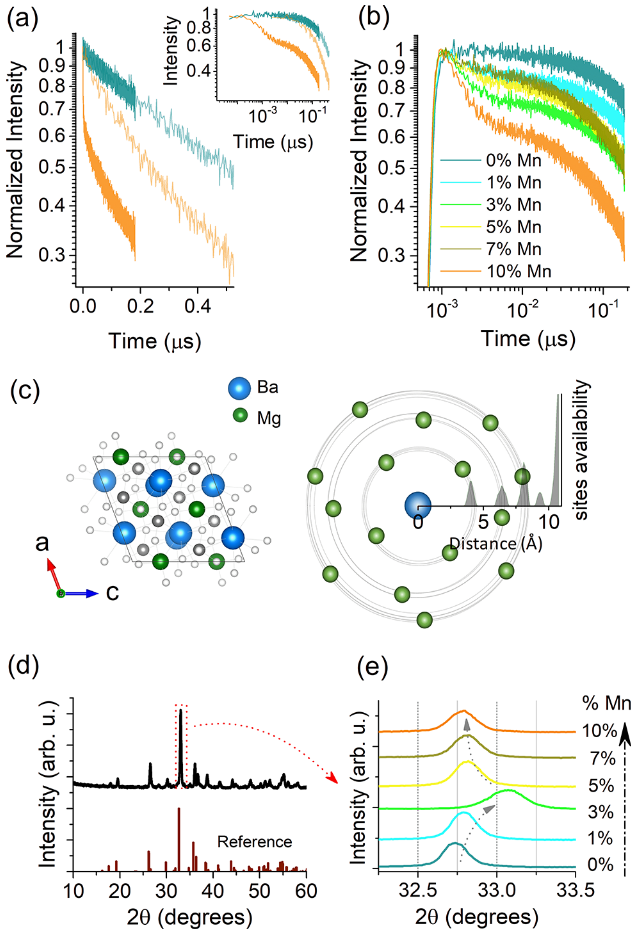

**Figure 3.** Luminescence decay curves of $Eu^{2+}$ emission in singly $Eu^{2+}$ doped (3.5%) and 10% $Mn^{2+}$ codoped $Ba_2MgSi_2O_7$ at 300 K for $\lambda_{em}$ = 470 nm and $\lambda_{exc}$ = 375 nm (a). High-resolution decay curve recorded with 0.048 ns channel width is plotted for the singly doped (dark cyan) and codoped (dark orange) compounds. For comparison, corresponding full time range "normal" decay curves (2.4 ns channel width) are presented in lower contrast. Inset of (a) shows decay curves in a log−log plot. High-resolution (0.048 ns channel width) decay curves for $Eu^{2+}$−$Mn^{2+}$ codoped $Ba_2MgSi_2O_7$ at 300 K in a log−log plot (b). $Ba_2MgSi_2O_7$ monoclinic lattice structure and corresponding Ba−Mg radial distribution (c). Powder XRD pattern of $Ba_2MgSi_2O_7$ (d) and enlarged view of a PXRD reflection in different $Eu^{2+}$−$Mn^{2+}$ codoped $Ba_2MgSi_2O_7$ compounds (e).

$Mn^{2+}$ codoped $Ba_2MgSi_2O_7$ compounds. The HR decay curves reveal that the codoped compound exhibits a very fast decay component, which is averaged out and thus goes undetected in "normal" low-resolution (LR) full time range decay curve measurement as shown in Figure 1e (channel width 2.4 ns). This fast component is not detected in HR decay of $Eu^{2+}$ singly doped compound, confirming that the fast component is not an instrumental artifact but is a signature of fast $Eu^{2+}$−$Mn^{2+}$ NN transfer. The inset in Figure 3a shows the decay curve in log−log scale and reveals that the fast decay component lies in the approximately nanoseconds range and is significantly slower than the instrument response function (IRF) of our detection system around 0.14 ns (Figures S2 and S3).

Figure 3b presents the $Eu^{2+}$ HR PL decay curves for different $Mn^{2+}$ codoped compounds in a log−log scale. Interestingly, the amplitude of the ∼1 ns decay component does not exhibit a linear dependence on $Mn^{2+}$ content. It first increases until 3% $Mn^{2+}$, is lower for 5% and 7% $Mn^{2+}$, and then again increases in the codoped compound with 10% $Mn^{2+}$. In contrast, at longer times (>1 µs), the decay becomes consistently faster with increasing $Mn^{2+}$ concentration (Figures 3b and 1e). This interesting observation is attributed to the microscopic dopant distribution in the lattice. The formation of dopant ion pairs, or more broadly an aggregation of impurity ions with deviating ionic radii, is commonly observed and explained by reducing lattice strain.[14,62] As $Eu^{2+}$ is smaller than $Ba^{2+}$ and $Mn^{2+}$ is larger than $Mg^{2+}$ in their respective coordination sites, they can be expected to preferentially substitute in close proximity to reduce local strain. Figure 3c shows the monoclinic crystal structure of $Ba_2MgSi_2O_7$ and the related Ba−Mg radial distribution. $Ba_2MgSi_2O_7$ exhibits monoclinic or tetragonal crystal structures,[63] where most polycrystalline powders are reported to crystallize in monoclinic structure with space group $C2/c$.[57−59] The structure is composed of discrete $[Si_2O_7]^{6-}$ units connected by tetrahedrally coordinated Mg ions, forming two-dimensional sheets in the *ac* plane and are separated by layers of octahedrally coordinated Ba ions. The radial distribution plot reveals the distance and number of available sites of tetrahedrally coordinated $Mg^{2+}$ ions around the octahedrally coordinated $Ba^{2+}$ ions in the monoclinic lattice of $Ba_2MgSi_2O_7$. Multiple shells of nonequidistant Mg sites are available for $Mn^{2+}$ ions around $Eu^{2+}$ ions occupying at the $Ba^{2+}$ octahedral site. The observation in HR decay kinetics hints that the $Mn^{2+}$ occupancies in these $Mg^{2+}$ sites are not statistically uniform for all the concentrations, but they prefer to form close to intermediate distance pairs with different weight probabilities depending on $Mn^{2+}$ concentrations or small variations in the synthesis procedure. Thus, it is anticipated that the pair formation and their distance distribution might be influenced by the elastic distortions in the lattice. Figure 3d shows powder X-ray diffraction (PXRD) pattern of $Ba_2MgSi_2O_7$. An enlarged view of a prominent X-ray peak (reflections due to (022), (13−1), and (220) planes) is presented in Figure 3e for different Mn codoping concentrations showing that the peak shift is not linear. In view of larger size of $Mn^{2+}$, a lattice expansion could be expected with $Mn^{2+}$ codoping, but the PXRD peak first shifts toward higher diffraction angles (contraction) until 3% and then shifts back upon further increase in doping concentrations (see also Figure S5). This is not in line with Vegard's law[64] and further confirms our hypothesis of a nonuniform $Eu^{2+}$−$Mn^{2+}$ distribution in the lattice and the observed nonlinear trend in the amplitude of the fast decay component.

Information on the energy transfer mechanism can be obtained from analysis of the $Eu^{2+}$ emission decay curves. The HR luminescence decay curves show a very fast initial decay component followed by a much slower decay. This characteristic shape is most clearly observed for the samples doped with 3% or 10% $Mn^{2+}$. A biexponential fit of the decay curves yields a very fast component of ∼1.6 ns and a slower component of ∼400 ns (see Figure S4 and Table S3). The second decay component is much slower than the fast initial decay but still faster than the radiative decay time of ∼800 ns. We ascribe these two decay components to energy transfer to $Mn^{2+}$ ions in the nearest-neighbors (NN) shell and to $Mn^{2+}$ in the next-nearest-neighbor (NNN) shell. The distances for $Eu^{2+}$ to NN $Mn^{2+}$ and NNN $Mn^{2+}$ ions can be calculated from the crystal structure data assuming $Eu^{2+}$ substitutes on $Ba^{2+}$ sites and $Mn^{2+}$ on $Mg^{2+}$ sites. The symmetry of the $Ba_2MgSi_2O_7$ crystal structure is low, and calculations of distances between $Ba^{2+}$

sites and the surrounding $Mg^{2+}$ sites are included in the Supporting Information (Table S4). There are four NNs at on average 4.1 Å and four NNNs at on average 6.4 Å. The energy transfer rates $k_{ET}$ ($k_{ET} = 1/\tau_{exp} - 1/\tau_{rad}$) calculated from the fast 1.6 ns initial decay yields $k_{ET} = 6.25 \times 10^8$ s$^{-1}$ and the slower 400 ns component corresponds to $k_{ET} = 1.25 \times 10^6$ s$^{-1}$, 500 times slower than the NN transfer rate. This strong distance dependence of $k_{ET}$ is characteristic of energy transfer by exchange interaction. For dipole−quadrupole interaction with a $r^{-8}$ distance dependence, energy transfer to NNN at 6.4 Å is expected to be a mere 35 times slower than transfer to NN at 4.1 Å. Using the NN transfer rate as a reference would give an estimate of $k_{ET} \sim 18 \times 10^6$ s$^{-1}$ for the NNN transfer rate, which is 15 times faster than the experimentally observed value of $1.25 \times 10^6$ s$^{-1}$. For energy transfer via exchange interaction an exponential dependence in agreement with the Dexter's exchange interaction is expected, following the expression[65]

$$k_{ET} \propto \exp\left(\frac{-2r}{l}\right) \tag{4}$$

Here, $r$ is average interionic separation and $l$ represents the effective Bohr radius (average effective Bohr radius of the donor excited state and acceptor ground state). With eq 4 and the 500-fold decrease in ET rate to $Mn^{2+}$ ions at 4.1 and 6.4 Å, the effective Bohr radius can be estimated to be ∼0.8 Å. This effective radius is in agreement with earlier reports on an effective radius of 0.67 Å for $Eu^{2+}$−$Mn^{2+}$ ET via exchange interaction and 0.55 Å found for $Sb^{3+}$ to $Mn^{2+}$ exchange-mediated ET.[10,28] Theoretical calculation of the effective Bohr radius is challenging as it is not possible to predict how much atomic orbitals expand (nephelauxetic effect) upon incorporation of ions into a host lattice.

On the basis of the strong evidence for Eu−Mn ET via exchange interaction, it is interesting to take a closer look at the overwhelming number of recent publications reporting dipole−quadrupole interaction as transfer mechanism. Over hundreds of publications in the past 15 years have investigated Eu−Mn or Ce−Mn energy transfer and conclude that the mechanism is dipole−quadrupole interaction, at odds with the present findings. The various publications have a similar structure and show plots of ratios of $Eu^{2+}$ emission intensities ($I_{S0}/I_S$), energy transfer efficiencies ($\eta_{S0}/\eta_S$), and/or $Eu^{2+}$ emission decay times ($\tau_{S0}/\tau_S$) for singly Eu doped phosphors (S0) vs Eu−Mn codoped phosphors (S). With reference to each other or sometimes to an original paper by Dexter and Schulman,[55] it is stated that these ratios are expected to increase with the $Mn^{2+}$ concentration $C$ proportional to $C^{6/3}$ (dipole−dipole), $C^{8/3}$ (dipole−quadrupole), or $C^{10/3}$ (quadrupole−quadrupole). Often the best fit was obtained for $C^{8/3}$, and a dipole−quadrupole ET mechanism was thus concluded.[32−54] Sometimes a better fit was found for $C^{6/3}$ or $C^{10/3}$ and was used to derive that dipole−dipole or quadrupole−quadrupole interaction was the operative transfer mechanism.[8,66−68] Finally, it is important to realize that these $C^{S/3}$ vs $I_{S0}/I_S$, $\eta_{S0}/\eta_S$, or $\tau_{S0}/\tau_S$ fitting methods to derive ET mechanisms are also widely used for other donor−acceptor pairs, for example, $Tb^{3+} \rightarrow Eu^{3+}$.[69] The $C^{S/3}$ model is widespread but, as will be shown below, incorrect for donor−acceptor energy transfer as it has been derived for concentration quenching by energy migration among donors.

It is somewhat surprising that the model derived by Dexter and Schulman[55] for the efficiency of energy transfer between donors to quenching centers (concentration quenching) is used to describe the concentration dependence of donor−acceptor energy transfer. Possibly the term "activators" for the "donors" used in ref 55 caused confusion and lead to the idea that the paper involved donor → activator/acceptor energy transfer. From the beginning of ref 55 it is however clear that the reported theory concerns concentration quenching by energy transfer between donors (or activators) to quenching centers, as the first line of the abstract reads "A theory is presented for concentration quenching in solid systems, based on the energy migration of excitation energy from one activator center to another and eventually to an imperfection which may act as an energy sink". Even without a careful study of ref 55 it should be evident that donor−acceptor energy transfer rates increase linearly with acceptor concentration and cannot follow a $C^{S/3}$ dependence with $S$ = 6, 8, or 10. The probability for a neighbor site (NN, NNN, NNNN, etc.) to be occupied by an acceptor increases linearly with acceptor concentration and thus so does the energy transfer rate.

To further prove this point, we did simulations for energy transfer via dipole−dipole, dipole−quadrupole, or quadrupole−quadrupole interaction in a model system using our shell model for ET.[70,71] The results are plotted in Figure 4. The donor−acceptor ET strength was chosen such that the ET rate was equal to the radiative decay rate at ∼1.8 times the NN distance as this corresponds to energy transfer efficiencies that resemble those observed in refs 47−54. Transfer efficiencies and donor emission decay curves were calculated and used to derive intensity ratios and lifetime ratios as a function of $C^{S/3}$. The results are shown in Figure 4a. For all interaction types, the plots are approximately linear over some range, but they all clearly deviate from linear in the limit of low concentrations. This is also visible in the $C^{S/3}$ vs $I_{S0}/I_S$ or $\tau_{S0}/\tau_S$ curves reported in the various papers.[27,48−54] The observation of an approximately linear behavior for a limited concentration range thus cannot serve to determine a $C^{S/3}$ dependence.

The proper method to determine the exponent of a theoretically predicted or expected power dependence is making a log−log plot. The slope in a log−log plot immediately gives the power dependence. In Figure 4b, the log−log plot of the energy transfer rate and energy transfer efficiency are shown for energy transfer simulations assuming dipole−dipole, dipole−quadrupole, or quadrupole−quadrupole interaction. As expected, theoretically a linear power dependence is found for the energy transfer rate, for any energy transfer mechanism. The modeling is based on a random distribution of acceptors. Intuitively, it is clear that the probability of finding an acceptor at a specific neighbor site linearly increases with the acceptor concentration. As $k_{ET}$ is determined by the sum of transfer rates to all acceptors for a specific configuration of acceptors around a donor, also $k_{ET}$ will increase linearly with acceptor concentration for a random acceptor distribution. The experimental effective energy transfer rates ($k_{ET}$) in the present $Ba_2MgSi_2O_7$ compound was obtained from the spectral energy transfer efficiency $\eta_{ET}$ via

$$k_{ET} = \frac{1}{\tau_D}\left(\frac{\eta_{ET}}{1 - \eta_{ET}}\right) \tag{5}$$

The experimentally observed concentration dependence of $k_{ET}$ is plotted in Figure 4c in a log−log plot. The slope of 1 indicates a linear dependence between $k_{ET}$ and $C_{Mn}$ as expected for a random $Mn^{2+}$ distribution. For the $Eu^{2+}$ to $Mn^{2+}$ ET there

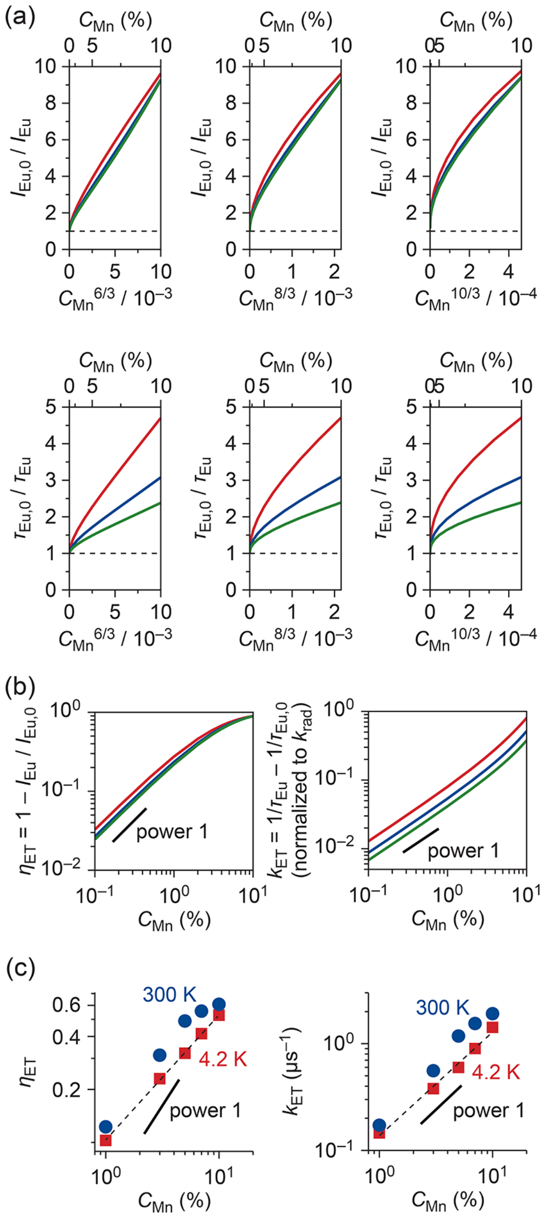

**Figure 4.** (a) Simulated plots of donor emission intensity ratio ($I_{Eu,0}/I_{Eu}$) and emission decay lifetime ratio ($\tau_{Eu,0}/\tau_{Eu}$) with acceptor concentration for dipole−dipole (red lines), dipole−quadrupole (blue lines), or quadrupole−quadrupole (green lines) interaction in a model system using the shell model for ET.[70,71] Subscripts "Eu,0" and "Eu" represent singly Eu doped and Eu−Mn codoped compound, respectively. (b) A log−log plot of simulated energy transfer efficiency ($\eta_{ET}$) and energy transfer rate ($k_{ET}$) as a function of acceptor concentration. The linear part with slope equal to unity is depicted by short black line. (c) A log−log plot of experimental data on $Eu^{2+}$−$Mn^{2+}$ energy transfer efficiency and energy transfer rate as a function of acceptor concentration in $Ba_2MgSi_2O_7$ compounds at 4.2 and 300 K. Dotted line presents a linear fit to the data points at 4.2 K. A short black solid line with slope equal to unity is drawn to guide the relative slope difference.

are strong indications that the $Mn^{2+}$ distribution is not random but that there is preferential pair formation. The observation of a linear dependence indicates that there may be a fixed fraction of the $Mn^{2+}$ ions that is prone to preferential pair formation. The amplitude of the fast initial part of the $Eu^{2+}$ decay curves, however, does not increase linearly with the $Mn^{2+}$ concentration, which is inconsistent with this suggestion and further research on the role of preferential Eu−Mn pair formation is needed. The extent of pair formation may also depend on subtle variations in the synthesis procedure and therefore not show a consistent trend within a concentration series because of unintended variations in the synthesis conditions.

Finally, the energy transfer efficiencies ($\eta_{ET}$) are plotted as a function of Mn concentration. The log−log plot in Figure 4b shows that theoretically a linear dependence is expected in the low acceptor concentration regime but starts to deviate as the transfer efficiencies increase above ∼10%. The experimentally observed concentration dependence for Eu → Mn ET efficiencies in $Ba_2MgSi_2O_7$ is shown in a log−log plot in Figure 4c. The results show a sublinear increase (slope ∼0.7). This slope is in agreement with the theoretically expected slope as we already are in the regime of transfer efficiencies between 5 and 20% where the increase is no longer linear with acceptor concentration.

## ■ CONCLUSION

In summary, we conclude that the $Eu^{2+}$ → $Mn^{2+}$ energy transfer mechanism is dominantly Dexter's exchange type interaction in $Ba_2MgSi_2O_7$ and probably also in most other $Eu^{2+}$−$Mn^{2+}$ codoped phosphors. Previous work reporting dipole−quadrupole interaction as the transfer mechanism relied on a presumed $C^{8/3}$ concentration dependence of the $Eu^{2+}$−$Mn^{2+}$ transfer efficiency ratio (or $Eu^{2+}$ emission intensity ratio or lifetime ratio) in singly Eu doped and Eu−Mn codoped phosphors with $Mn^{2+}$ concentration $C$. It is argued here that this model is incorrect and that in fact a linear $C$ dependence is expected and observed for donor−acceptor ET rates, independent of transfer mechanism. The model yielding a $C^{8/3}$ concentration dependence was derived for energy transfer efficiency ratios for transfer to quenching centers by concentration quenching through donor−donor, *not* donor−acceptor, transfer where $C$ is donor concentration, not the acceptor concentration.

Strong evidence for the exchange interaction mechanism is provided by analysis of high-resolution luminescence decay curves of the $Eu^{2+}$ emission in Eu−Mn codoped phosphors. These decays show the signature of exchange interaction: a very fast initial decay for NN transfer followed by a much slower decay for NNN transfer. The energy transfer to NN $Mn^{2+}$ at 4.1 Å is ∼500 times faster than ET to NNN neighbors at 6.4 Å. This steep distance dependence does not fit the dipole−quadrupole interaction but is consistent with the strong distance dependence for exchange interaction with an effective Bohr radius of ∼0.8 Å for Dexter ET. In line with earlier reports, there are indications that the distribution of $Eu^{2+}$ and $Mn^{2+}$ in the host lattice is not random but that preferential Eu−Mn pair formation helps to improve the ET efficiency. The present insights are important in the design of new narrow-band red or green phosphors based on sensitized $Mn^{2+}$ emission. Efficient sensitization is only possible in host lattices with a short (<5 Å) $Eu^{2+}$−$Mn^{2+}$ or $Ce^{3+}$−$Mn^{2+}$ distance and will benefit from preferential pair formation.

## ■ ASSOCIATED CONTENT

### SI Supporting Information

The Supporting Information is available free of charge at https://pubs.acs.org/doi/10.1021/acs.jpcc.0c03425.

PL decay curve fits, decay LT calculation, energy transfer efficiency calculation, instrument response function (IRF), high-resolution decay components, Ba−Mg separation in monoclinic host lattice, and enlarged PXRD patterns of codoped samples (PDF)

## ■ AUTHOR INFORMATION

### Corresponding Authors

**Atul D. Sontakke** − *Condensed Matter & Interfaces, Debye Institute for Nanomaterials Science, Utrecht University, 3584 CC Utrecht, The Netherlands;* orcid.org/0000-0001-5132-0942; Email: a.d.sontakke@uu.nl

**Andries Meijerink** − *Condensed Matter & Interfaces, Debye Institute for Nanomaterials Science, Utrecht University, 3584 CC Utrecht, The Netherlands;* orcid.org/0000-0003-3573-9289; Email: a.meijerink@uu.nl

### Authors

**Arnoldus J. van Bunningen** − *Condensed Matter & Interfaces, Debye Institute for Nanomaterials Science, Utrecht University, 3584 CC Utrecht, The Netherlands*

**Freddy T. Rabouw** − *Condensed Matter & Interfaces, Debye Institute for Nanomaterials Science, Utrecht University, 3584 CC Utrecht, The Netherlands;* orcid.org/0000-0002-4775-0859

**Sam Meijers** − *Condensed Matter & Interfaces, Debye Institute for Nanomaterials Science, Utrecht University, 3584 CC Utrecht, The Netherlands*

Complete contact information is available at:
https://pubs.acs.org/10.1021/acs.jpcc.0c03425

### Notes

The authors declare no competing financial interest.

## ■ ACKNOWLEDGMENTS

Financial support from Nichia Corporation (Japan) is gratefully acknowledged.

## ■ REFERENCES

(1) Murphy, J. E.; Beers, W.; Butts, M.; Camardello, S. J.; Chowdhury, A.; Cohen, W.; Du, F.; Liu, J.; Nelson, C.; Parthasarathy, G.; et al. Narrow Band Emitting LED Phosphors for Wide Color Gamut Displays & Energy Efficient SSL. *2018 IEEE Photonics Conference (IPC)*, Reston, VA, Sept 30−Oct 04, 2018; pp 1−1.

(2) van de Haar, M. A.; Berends, A. C.; Krames, M. R.; Chepyga, L.; Rabouw, F. T.; Meijerink, A. $Eu^{3+}$ Sensitization via Nonradiative Interparticle Energy Transfer Using Inorganic Nanoparticles. *J. Phys. Chem. Lett.* **2020**, *11*, 689−695.

(3) Hoerder, G. J.; Seibald, M.; Baumann, D.; Schröder, T.; Peschke, S.; Schmid, P. C.; Tyborsky, T.; Pust, P.; Stoll, I.; Bergler, M.; et al. $Sr[Li_2Al_2O_2N_2]:Eu^{2+}$-A High Performance Red Phosphor to Brighten the Future. *Nat. Commun.* **2019**, *10*, 1824.

(4) Yoshimura, K.; Fukunaga, H.; Izumi, M.; Takahashi, K.; Xie, R.-J.; Hirosaki, N. Achieving Superwide-Color-Gamut Display by Using Narrow-Band Green-Emitting γ-AlON:Mn, Mg Phosphor. *Jpn. J. Appl. Phys.* **2017**, *56*, 041701.

(5) Cherepy, N. J.; Payne, S. A.; Harvey, N. M.; Åberg, D.; Seeley, Z. M.; Holliday, K. S.; Tran, I. C.; Zhou, F.; Martinez, H. P.; Demeyer, J. M.; et al. Red-Emitting Manganese-Doped Aluminum Nitride Phosphor. *Opt. Mater.* **2016**, *54*, 14−21.

(6) Setlur, A. A.; Shiang, J. J.; Happek, U. $Eu^{2+}$-$Mn^{2+}$Phosphor Saturation in 5 mm Light Emitting Diode Lamps. *Appl. Phys. Lett.* **2008**, *92*, 081104.

(7) Zhang, J.; Jiang, C. Photoluminescence Propoerties of Emission-Tunable $Ca_8MgLa(PO_4)_7:Eu^{2+}$, $Mn^{2+}$ Phosphors for White LEDs. *Opt. Mater. Express* **2014**, *4*, 2102−2107.

(8) Si, J.; Wang, L.; Liu, L.; Yi, W.; Cai, G.; Takeda, T.; Funahashi, S.; Hirosaki, N.; Xie, R.-J. Structure, Luminescence and Energy Transfer in $Ce^{3+}$ and $Mn^{2+}$ codoped γ-AlON Phosphors. *J. Mater. Chem. C* **2019**, *7*, 733−742.

(9) Masai, H.; Hino, Y.; Yanagida, T.; Fujimoto, Y.; Tokuda, Y. High Energy-Transfer Rate From $Sn^{2+}$ to $Mn^{2+}$ in Phosphate Glasses. *Opt. Mater. Express* **2015**, *5*, 617−622.

(10) Soules, T. F.; Bateman, R. L.; Hewes, R. A.; Kreidler, E. R. Energy Transfer Between Antimony and Manganese in the Fluorophosphate Phosphors. *Phys. Rev. B* **1973**, *7*, 1657.

(11) Matsuyama, I.; Yamashita, N.; Nakamura, K. Photoluminescence of the $SrS:Mn^{2+}$ Phosphor and $Pb^{2+}$-Sensitized Luminescence of the $SrS:Pb^{2+}$, $Mn^{2+}$ Phosphor. *J. Phys. Soc. Jpn.* **1989**, *58*, 741−751.

(12) Majher, J. D.; Gray, M. B.; Strom, T. A.; Woodward, P. M. $Cs_2NaBiCl_6:Mn^{2+}$-A New Orange-Red Halide Double Perovskite Phosphor. *Chem. Mater.* **2019**, *31*, 1738−1744.

(13) Stevels, A. L. N.; Verstegen, J. M. P. J. $Eu^{2+}$ → $Mn^{2+}$ Energy Transfer in Hexagonal Aluminates. *J. Lumin.* **1976**, *14*, 207−218.

(14) Rubio, J. O.; Murrieta, S. H.; Powell, R. C.; Sibley, W. A. $Eu^{2+}$ → $Mn^{2+}$ Energy Transfer in NaCl. *Phys. Rev. B: Condens. Matter Mater. Phys.* **1985**, *31*, 59.

(15) Rubio, J. O.; Munoz, A. F.; Monoz, G. H.; Lopez-Morales, M. E. On the Mechanism of Eu→Mn Energy Transfer in Monocrystalline NaCl. *J. Phys. C: Solid State Phys.* **1988**, *21*, 2059.

(16) Shinn, M. D.; Sibley, W. A. $Eu^{2+}$-Sensitized $Mn^{2+}$ Luminescence in $PbMgF_3$:Eu, Mn. *Phys. Rev. B: Condens. Matter Mater. Phys.* **1984**, *29*, 3834.

(17) Kunimoto, T.; Fujita, Y.; Kajiyama, H.; Honma, T.; Kawaguchi, H.; Ishigaki, T.; Ohmi, K.; Ohshima, K.; Miyazaki, D.; Saito, Y.; et al. Development of $Eu^{2+}$ and $Mn^{2+}$ Co-activated Silicate Phosphor for Plant Cultivation Light Source. *Jpn. J. Appl. Phys.* **2019**, *58*, SFFD03.

(18) Shi, R.; Ning, L.; Wang, Z.; Chen, J.; Sham, T.-K.; Huang, Y.; Qi, Z.; Li, C.; Tang, Q.; Liang, H. Zero-Thermal Quenching of $Mn^{2+}$ Red Luminescence via Efficient Energy Transfer from $Eu^{2+}$ in $BaMgP_2O_7$. *Adv. Opt. Mater.* **2019**, *7*, 1901187.

(19) Zhang, Z.; Ma, C.; Gautier, R.; Molokeev, M. S.; Liu, Q.; Xia, Z. Structural Confinement Towards Gaint Enhancement of Red Emission in $Mn^{2+}$-Based Phosphors. *Adv. Funct. Mater.* **2018**, *28*, 1804150.

(20) Zhou, J.; Liu, Q.; Xia, Z. Structural Construction and Photoluminescence Tuning via Energy Transfer in Apatite-Type Solid-State Phosphors. *J. Mater. Chem. C* **2018**, *6*, 4371−4383.

(21) Yun, Y. J.; Kim, J. K.; Ju, J. Y.; Choi, S. K.; Park, W. I.; Suh, J. Y.; Jung, H.-k.; Kim, Y.; Choi, S. Dual Spectra Band Emissive $Eu^{2+}$/$Mn^{2+}$ Co-activated Alkaline Earth Phosphates for Indoor Plant Growth Novel Phosphor Converted-LEDs. *Phys. Chem. Chem. Phys.* **2017**, *19*, 11111−11119.

(22) Sun, Y.; Li, P.; Wang, Z.; Cheng, J.; Li, Z.; Wang, C.; Tian, M.; Yang, Z. Tunable Emission Phosphor $Ca_{0.75}Sr_{0.2}Mg_{1.05}(Si_2O_6):Eu^{2+}$, $Mn^{2+}$: Luminescence and Mechanism of Host, Energy Transfer of $Eu^{2+}$ → $Mn^{2+}$, $Eu^{2+}$ → Host, and Host→$Mn^{2+}$. *J. Phys. Chem. C* **2016**, *120*, 20254−20266.

(23) Li, M.; Zhang, J.; Han, J.; Qiu, Z.; Zhou, W.; Yu, L.; Li, Z.; Lian, S. Changing $Ce^{3+}$ Contents and Codoping $Mn^{2+}$ Induced Tunable Emission and Energy Transfer in $Ca_{2.5}Sr_{0.5}Al_2O_6:Ce^{3+}$, $Mn^{2+}$. *Inorg. Chem.* **2017**, *56*, 241−252.

(24) Han, J. K.; Piqutte, A.; Hannah, M. E.; Hirata, G. A.; Talbot, J. B.; Mishra, K. C.; McKittrick, J. Analysis of (Ba, Ca, $Sr)_3MgSi_2O_8:Eu^{2+}$, $Mn^{2+}$ Phosphors for Application in Solid State Lighting. *J. Lumin.* **2014**, *148*, 1−5.

(25) Puchalska, M.; Zych, E. $Ce^{3+}$-Sensitized Red $Mn^{2+}$ Luminescence in Calcium Aluminoborate Phosphor Material. *Opt. Mater.* **2017**, *74*, 2−11.

(26) Feng, L.; Hao, Z.; Zhang, X.; Zhang, L.; Pan, G.; Luo, Y.; Zhang, L.; Zhao, H.; Zhang, J. Red Emission Generation Through

Highly Efficient Energy Transfer from $Ce^{3+}$ to $Mn^{2+}$ in CaO for Warm White LEDs. *Dalton. Trans.* **2016**, *45*, 1539−1545.

(27) Müller, M.; Fischer, S.; Justel, T. Luminescence and Energy Transfer of Co-doped $Sr_5MgLa_2(BO_3)_6$:$Ce^{3+}$, $Mn^{2+}$. *RSC Adv.* **2015**, *5*, 67979−67987.

(28) Happek, U.; Setlur, A. A.; Shiang, J. J. Inverse Bottleneck in $Eu^{2+}$-$Mn^{2+}$ Energy Transfer. *J. Lumin.* **2009**, *129*, 1459−1463.

(29) Park, C.-Y.; Park, S. Luminescence Property of $Eu^{2+}$, $Mn^{2+}$ Co-doped $Y_7O_6F_9$ Phosphors. *J. Lumin.* **2016**, *178*, 463−469.

(30) Xu, Y.; Li, X.; Feng, W.; Li, W.; Zhang, K. Luminescence and Energy Transfers Properties of Novel $Na_{2.5}Y_{0.5}Mg_7(PO_4)_6$: R (R = $Eu^{2+}$, $Tb^{3+}$ and $Mn^{2+}$) Phosphors. *Dalton Trans.* **2016**, *45*, 3983−3991.

(31) Mi, R.; Zhao, C.; Xia, Z. Synthesis, Structure, and Tunable Luminescence Properties of Novel $Ba_3NaLa(PO_4)_3F$:$Eu^{2+}$, $Mn^{2+}$ Phosphors. *J. Am. Ceram. Soc.* **2014**, *97*, 1802−1808.

(32) Caldino, G. U. Energy Transfer in $CaF_2$ Doped with $Ce^{3+}$, $Eu^{2+}$ and $Mn^{2+}$ Ions. *J. Phys.: Condens. Matter* **2003**, *15*, 7127−7137.

(33) Liang, S.; Dang, P.; Li, G.; Molokeev, M. S.; Wei, Y.; Wei, Y.; Lian, H.; Shang, M.; Al Kheraif, A. A.; Lin, J. Controllable Two-Dimensional Luminescence Tuning in $Eu^{2+}$, $Mn^{2+}$ Doped (Ca, $Sr)_9Sc(PO_4)_7$ Based on Crystal Field Regulation and Energy Transfer. *J. Mater. Chem. C* **2018**, *6*, 6714−6725.

(34) Huo, J.; Zhu, Q.; Li, S.; Gao, J.; Wang, Q. Effective Assembly of a Novel Aluminum-Oxynitride $BaAl_{11}O_{16}N$ Activated by $Eu^{2+}$ and $Mn^{2+}$ via Salt-Flux Assistance and Its Photophysical Investigation. *J. Alloys Compd.* **2019**, *787*, 96−103.

(35) Zhang, J.; Zhang, X.; Zhang, J.; Ma, W.; Ji, X.; Liao, S.; Qiu, Z.; Zhou, W.; Yu, L.; Lian, S. Near-UV-to-Red Light Conversion Through Energy Transfer in $Ca_2Sr(PO_4)_2$:$Ce^{3+}$, $Mn^{2+}$ for Plant Growth. *J. Mater. Chem. C* **2017**, *5*, 12069−12076.

(36) Yan, J.; Zhang, Z.; Wen, D.; Zhou, J.; Xu, Y.; Li, J.; Ma, C.-G.; Shi, J.; Wu, M. Crystal Structure and Photoluminescence Tuning of Novel Single-Phase $Ca_8ZnLu(PO_4)_7$:$Eu^{2+}$, $Mn^{2+}$ Phosphors for Near-UV Converted White Light-Emitting Diodes. *J. Mater. Chem. C* **2019**, *7*, 8374−8382.

(37) Cui, M.; Wang, J.; Shang, M.; Li, J.; Wei, Q.; Dang, P.; Jang, H. S.; Lin, J. Full Visible Light Emission in $Eu^{2+}$, $Mn^{2+}$-Doped $Ca_9LiY_{0.667}(PO_4)_7$ Phosphors Based on Multiple Crystal Lattice Substitution and Energy Transfer for Warm White LEDs with High Color-Rendering. *J. Mater. Chem. C* **2019**, *7*, 3644−3655.

(38) Long, J.; Wang, Y.; Ma, C.; Yuan, X.; Dong, W.; Ma, R.; Wen, Z.; Du, M.; Cao, Y. Photoluminescence Tuning of $Ca_{8-x}Sr_xMgGd(PO_4)_7$:$Eu^{2+}$, $yMn^{2+}$ Phosphors for Applications in White LEDs with Excellent Color Rendering Index. *RSC Adv.* **2017**, *7*, 19223−19230.

(39) Jiao, M.; Xu, Q.; Yang, C.; Liu, M. Electronic Structure and Photoluminescence Properties of Single Component White Emitting $Sr_3LuNa(PO_4)_3F$:$Eu^{2+}$, $Mn^{2+}$ Phosphor for WLEDs. *J. Mater. Chem. C* **2018**, *6*, 4435−4443.

(40) Wang, Y.; Zhang, J.; Shi, J.; Jiao, H. Luminescence Properties of $(Sr_{0.86}Mg_{0.14})_3(PO_4)_2$: $Eu^{2+}$, $Mn^{2+}$ Phosphors for LEDs Application. *J. Mater. Sci.: Mater. Electron.* **2017**, *28*, 8895.

(41) Zhang, B.; Ying, S.; Wang, S.; Han, L.; Zhang, J.; Chen, B. Blue-Green-Yellow Color-Tunable Luminescence of $Ce^{3+}$-, $Tb^{3+}$-, and $Mn^{2+}$-Codoped $Sr_3YNa(PO_4)_3F$ via Efficient Energy Transfer. *Inorg. Chem.* **2019**, *58*, 4500−4507.

(42) Xu, H.; Wang, L.; Qu, D.; Si, Z.; Shi, J. Structure and Photoluminescence Properties of Novel $Sr_6Ca_4(PO_4)_6F_2$:Re (Re = $Eu^{2+}$, $Mn^{2+}$) Phosphors with Energy Transfer for White-Emitting LEDs. *RSC Adv.* **2017**, *7*, 41282−41288.

(43) Zhou, W.; Han, J.; Pan, F.; Zhang, J.; Xie, Q.; Lian, S.; Yu, L.; Wang, J. Preparation and Luminescence Properties of $Eu^{2+}$ and $Mn^{2+}$ Coactivated Tricalcium Phosphate Phosphors. *J. Am. Ceram. Soc.* **2014**, *97*, 3631−3635.

(44) Dong, X.; Zhang, J.; Zhang, L.; Zhang, X.; Hao, Z.; Luo, Y. Yellow-Emitting $Sr_9Sc(PO_4)_7$:$Eu^{2+}$, $Mn^{2+}$ Phosphor with Energy Transfer for Potential Application in White Light-Emitting Diodes. *Eur. J. Inorg. Chem.* **2014**, *2014*, 870−874.

(45) Kwon, S. H.; Moon, B. K.; Choi, B. C.; Jeong, J. H.; Kim, J. H. Synthesis and Luminescent Properties of $CaAl_2Si_2O_8$:$Eu^{2+}$, $Mn^{2+}$ Phosphors for White LED. *J. Korean Phys. Soc.* **2016**, *68*, 363−367.

(46) Jiang, L.; Pang, R.; Li, D.; Sun, W.; Jia, Y.; Li, H.; Fu, J.; Li, C.; Zhang, S. Tri-Chromatic White-Light Emission from a Single-Phase $Ca_9Sc(PO_4)_7$:$Eu^{2+}$, $Tb^{3+}$, $Mn^{2+}$ Phosphor for LED Application. *Dalton Trans.* **2015**, *44*, 17241−17250.

(47) Guo, N.; Huang, Y.; You, H.; Yang, M.; Song, Y.; Liu, K.; Zheng, Y. $Ca_9Lu(PO_4)_7$:$Eu^{2+}$, $Mn^{2+}$: A Potential Single-Phased White-Light-Emitting Phosphor Suitable for White-Light-Emitting Diodes. *Inorg. Chem.* **2010**, *49*, 10907−10913.

(48) Huang, C.-H.; Chen, T.-M.; Liu, W.-R.; Chiu, Y.-C.; Yeh, Y.-T.; Jang, S.-M. A Single-Phased Emission-Tunable Phosphor $Ca_9Y(PO_4)_7$:$Eu^{2+}$, $Mn^{2+}$ with Efficient Energy Transfer for White-Light-Emitting Diodes. *ACS Appl. Mater. Interfaces* **2010**, *2*, 259−264.

(49) Huang, C.-H.; Liu, W.-R.; Chen, T.-M. Single-Phased White-Light Phosphor $Ca_9Gd(PO_4)_7$:$Eu^{2+}$, $Mn^{2+}$ Under Near-Ultraviolet Excitation. *J. Phys. Chem. C* **2010**, *114*, 18698−18701.

(50) Yang, W.-J.; Luo, L.; Chen, T.-M.; Wang, N.-S. Luminescence and Energy Transfer of Eu- and Mn-Coactivated $CaAl_2Si_2O_8$ as a Potential Phosphor for White-Light UVLED. *Chem. Mater.* **2005**, *17*, 3883−3888.

(51) Ke, W.-C.; Lin, C. C.; Liu, R.-S.; Kuo, M.-C. Energy Transfer and Significant Improvement Moist Stability of $BaMgAl_{10}O_{17}$: $Eu^{2+}$, $Mn^{2+}$ as a Phosphor for White Light-Emitting Diodes. *J. Electrochem. Soc.* **2010**, *157*, J307.

(52) Li, K.; Geng, D.; Shang, M.; Zhang, Y.; Lian, H.; Lin, J. Color-Tunable Luminescence and Energy Transfer Properties of $Ca_9Mg(PO_4)_7$:$Eu^{2+}$, $Mn^{2+}$ Phosphors for UV-LEDs. *J. Phys. Chem. C* **2014**, *118*, 11026−11034.

(53) Guo, N.; You, H.; Song, Y.; Yang, M.; Liu, K.; Zheng, Y.; Huang, Y.; Zhang, H. White-Light Emission from a Single-Emitting-Component $Ca_9Gd(PO_4)_7$:$Eu^{2+}$, $Mn^{2+}$ Phosphor with Tunable Luminescent Properties for Near-UV Light-Emitting Diodes. *J. Mater. Chem.* **2010**, *20*, 9061−9067.

(54) Liu, W.-R.; Huang, C.-H.; Yeh, C.-W.; Tsai, J.-C.; Chiu, Y.-C.; Yeh, Y.-T.; Liu, R.-S. A Study on the Luminescence and Energy Transfer of Single-Phase and Color-Tunable $KCaY(PO_4)_2$:$Eu^{2+}$, $Mn^{2+}$ Phosphor for Application in White-Light LEDs. *Inorg. Chem.* **2012**, *51*, 9636−9641.

(55) Dexter, D. L.; Schulman, J. H. Theory of Concentration Quenching in Inorganic Phosphors. *J. Chem. Phys.* **1954**, *22*, 1063−1070.

(56) Dexter, D. L. A Theory of Sensitized Luminescence in Solids. *J. Chem. Phys.* **1953**, *21*, 836−850.

(57) Yan, J.; Ning, L.; Huang, Y.; Li, C.; Liu, C.; Hou, D.; Zhang, B.; Huang, Y.; Tao, Y.; Liang, H. Luminescence and Electronic Properties of $Ba_2MgSi_2O_7$:$Eu^{2+}$: A Combined Experimental and Hybrid Density Functional Theory Study. *J. Mater. Chem. C* **2014**, *2*, 8328−8332.

(58) Yan, J.; Liu, C.; Vlieland, J.; Zhou, J.; Dorenbos, P.; Huang, Y.; Tao, Y.; Liang, H. Intense Emission of $Ba_2MgSi_2O_7$:$Eu^{2+}$ Under X-ray Excitation for Potential Detecting Applications. *J. Lumin.* **2017**, *183*, 97−101.

(59) Yan, J.; Brik, M. G.; Liu, C.; Hou, D.; Zhou, W.; Zhang, B.; Huang, Y.; Tao, Y.; Liang, H. VUV-Vis Photoluminescence, Low-Voltage Cathodoluminescence and Electron-Vibrational Interaction of $Mn^{2+}$ in $Ba_2MgSi_2O_7$. *Opt. Mater.* **2015**, *43*, 59−65.

(60) Henderson, B.; Imbusch, G. F. *Optical Spectroscopy of Inorganic Solids*; Oxford University Press: Oxford, UK, 1989.

(61) de Jong, M.; Seijo, L.; Meijerink, A.; Rabouw, F. T. Resolving the Ambiguity in the Relation between Stokes shift and Huang-Rhys Parameter. *Phys. Chem. Chem. Phys.* **2015**, *17*, 16959−16969.

(62) Sontakke, A. D.; Annapurna, K. Energy Transfer Kinetics in Oxy-Fluoride Glass and Glass-Ceramics Doped with rare-Earth ions. *J. Appl. Phys.* **2012**, *112*, 013510.

(63) Aitasalo, T.; Hölsä, J.; Laamanen, T.; Lastusaari, M.; Lehto, L.; Niittykoski, J.; Pellé, F. Crystal Structure of the Monoclinic $Ba_2MgSi_2O_7$ Persistent Luminescence Material. *Z. Kristallogr. Suppl.* **2006**, *2006*, 481−486.

(64) Denton, A. R.; Ashcroft, N. W. Vegard's Law. *Phys. Rev. A: At., Mol., Opt. Phys.* **1991**, *43*, 3161−3164.

(65) Meares, C. F.; Yeh, S. M. Exchange Interaction Contribution to Energy Transfer Between Ions in the Rapid-Diffusion Limit. *J. Am. Chem. Soc.* **1981**, *103*, 1607−1609.

(66) Dong, Q.; Yang, F.; Cui, J.; Ming, H.; Du, F.; Peng, J.; Tian, Y.; Yang, S.; Ye, X. Small Thermal Quenching, Narrow Green Emitting γ-AlON: $Ce^{3+}$, $Mn^{2+}$ Phosphor: Luminescence and Energy Transfer. *ECS J. Solid State Sci. Technol.* **2018**, *7*, R215.

(67) Miao, S.; Xia, Z.; Zhang, J.; Liu, Q. Increased $Eu^{2+}$ Contents and Codoping $Mn^{2+}$ Induced Tunable Full-Color Emitting Phosphor $Ba_{1.55}Ca_{0.45}SiO_4$:$Eu^{2+}$, $Mn^{2+}$. *Inorg. Chem.* **2014**, *53*, 10386−10393.

(68) Liu, L.; Wang, L.; Zhang, C.; Cho, Y.; Dierre, B.; Hirosaki, N.; Sekiguchi, T.; Xie, R.-J. Strong Energy-Transfer-Induced Enhancement of Luminescence Efficiency of $Eu^{2+}$- and $Mn^{2+}$-Codoped Gamma-AlON for Near-UVLED-Pumped Solid State Lighting. *Inorg. Chem.* **2015**, *54*, 5556−5565.

(69) Back, M.; Boffelli, M.; Massari, A.; Marin, R.; Enrichi, F.; Riello, P. Energy Transfer Between $Tb^{3+}$ and $Eu^{3+}$ in Co-Doped $Y_2O_3$ Nanocrystals Prepared by Pechini Method. *J. Nanopart. Res.* **2013**, *15*, 1753.

(70) Rabouw, F. T.; den Hartog, S. A.; Senden, T.; Meijerink, A. Photonic Effects on the Förster Resonance Energy Transfer Efficiency. *Nat. Commun.* **2014**, *5*, 3610.

(71) Yu, D. C.; Rabouw, F. T.; Boon, W. Q.; Kieboom, T.; Ye, S.; Zhang, Q. Y.; Meijerink, A. Insights Into the Energy Transfer Mechanism in $Ce^{3+}$ - $Yb^{3+}$ Codoped YAG Phosphors. *Phys. Rev. B: Condens. Matter Mater. Phys.* **2014**, *90*, 165126.

https://dx.doi.org/10.1021/acs.jpcc.0c03425
*J. Phys. Chem. C* 2020, 124, 13902−13911